ADVANCED FUNCTIONAL MATERIALS
www.afm-journal.de

Investigating the Superoxide Formation and Stability in Mesoporous Carbon Perovskite Solar Cells with an Aminovaleric Acid Additive

*Emmanuel V. Péan, Catherine S. De Castro, Stoichko Dimitrov, Francesca De Rossi, Simone Meroni, Jenny Baker, Trystan Watson, and Matthew L. Davies**

Perovskite solar cells have attracted a great deal of attention thanks to their high efficiency, ease of manufacturing, and potential low cost. However, the stability of these devices is considered their main drawback and needs to be addressed. Mesoporous carbon perovskite solar cells (m-CPSC), consisting of three mesoporous layers (TiO_2/ZrO_2/C) infiltrated with $CH_3NH_3PbI_3$ (MAPI) perovskite, have presented excellent lifetimes of more than 10 000 h when the additive $NH_2(CH_2)_4CO_2HI$ (5- aminovaleric acid iodide; 5-AVAI) is used to modify the perovskite structure. Yet, the role of 5-AVAI in enhancing the stability has yet to be determined. Here, superoxide-mediated degradation of MAPI m-CPSC with and without the 5-AVAI additive is studied using the fluorescence probe dihydroethidium for superoxide detection. In situ X-ray diffractometry shows that aminovaleric acid methylammonium lead iodide (AVA-MAPI) perovskite infiltrated in mesoporous layers presents higher stability in an ambient environment under illumination, evidenced by a slower decrease of the MAPI/PbI_2 peak ratio. Superoxide yield measurements demonstrate that AVA-MAPI generates more superoxide than regular MAPI when deposited on glass but generates significantly less when infiltrated in mesoporous layers. It is believed that superoxide formation in m-CPSC is dependent on a combination of competitive factors including oxygen diffusion, sample morphology, grain size, and defect concentration.

1. Introduction

Halide perovskite solar cells (PSCs) have attracted great interest in the past decade thanks to their excellent optical properties, high carrier mobility, and diffusion length producing photovoltaic devices with relatively high power conversion efficiency (PCE).[1–3] Since the first report of a perovskite modified dye-sensitized solar cell achieving a 3.8% PCE,[4] a number of architectures and perovskite materials have been studied in an effort to improve the lifetime and performance of devices.[2,5–10] This has led to an impressive 25.2% PCE in 2019[3] giving merit for commercialization of this technology. However, the stability of PSCs needs to be addressed to realize the goal of mass production. PSCs can exhibit poor stability (of the order of days to weeks without encapsulation) due to degradation of the perovskite layer caused by moisture, oxygen, light, and combinations of these.[11–18] In the case of methylammonium lead iodide ($CH_3NH_3PbI_3$, MAPI) perovskite, it has been shown that water hydrates MAPI leading to conversion into methylammonium iodide (MAI) and lead iodide (PbI_2).[11–13] UV light can as well degrade perovskites through the photocatalytic effect of the mesoporous titanium dioxide layer in PSCs.[16]

More recently, superoxide-mediated degradation has been identified as a significant contributor to degradation, aided by relatively quick diffusion of O_2 in the perovskite ($\approx 10^{-7}$–10^{-9} cm^2 s^{-1}, meaning that oxygen can completely diffuse into a 2 µm perovskite film in less than 20 s).[14,15,18–21] Superoxide is formed when an excited electron, in the perovskite's conduction band, reduces molecular oxygen.[14] Iodide vacancies, acting as trap states in the perovskite bandgap, have been shown to be energetically favorable sites for the formation of superoxide when occupied by a trapped electron.[15,18,21] The formation of superoxide leads to the passivation of iodide vacancy trap states, reducing non-radiative recombination and therefore photobrightening the perovskite prior to superoxide-mediated degradation of the perovskite.[22] Smaller grains tend to generate more superoxide than larger grains.[15] The density of surface vacancies, which are well known to be more reactive than bulk

E. V. Péan, Dr. C. S. De Castro,[+] Dr. S. Dimitrov,[++] Dr. F. De Rossi, S. Meroni, Dr. J. Baker, Prof. T. Watson, Dr. M. L. Davies
SPECIFIC IKC
Materials Research Centre
College of Engineering
Swansea University Bay Campus
Fabian Way, Swansea SA1 8EN, UK
E-mail: m.l.davies@swansea.ac.uk

The ORCID identification number(s) for the author(s) of this article can be found under https://doi.org/10.1002/adfm.201909839.

[+]Present address: KAUST Solar Center KSC, Al-Kindi Bldg (5), Level 3, Room 3204-WS15, Thuwal 23955-6900, Kingdom of Saudi Arabia
[++]Present address: School of Biological and Chemical Sciences, Queen Mary University of London, London E1 4NS, UK

DOI: 10.1002/adfm.201909839

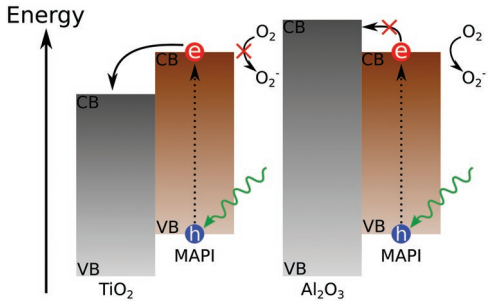

Figure 1. Superoxide formation in MAPI. If the conduction band minimum (CBM) of the electron transport layer (ETL) has a lower energy than the CBM of the perovskite, the electron can be injected in the ETL (left). In the opposite case, the photoelectron can react with molecular oxygen present in the air to form superoxide (right).

vacancies, have been estimated to be around 2.5 times higher in smaller crystals than larger ones due to their higher surface/volume ratio (6.0×10^{17} cm^{-3} and 2.4×10^{17} cm^{-3}, respectively).[15] Furthermore, it was estimated that the concentration of iodide vacancies in the bulk is around 10^{22} cm^{-3} making the bulk a significant contributor to superoxide formation as the shorter diffusion length of smaller crystals allows the O_2 molecule to reach the bulk defects faster.[23] The charge extraction rate and consequently, the mesoporous scaffold supporting the perovskite play an important role in superoxide formation in PSCs.[14] If the perovskite is deposited onto an insulator (e.g., aluminum oxide, Al_2O_3), then the excited state electrons are not injected into/extracted by the scaffold and thus they are more likely to react with molecular oxygen to form superoxide which can then degrade the perovskite (**Figure 1**). If the perovskite is deposited on a moderate bandgap semiconductor (e.g., titanium oxide, TiO_2), electrons can be extracted at a faster rate than the rate of the reaction with oxygen reducing the quantity of superoxide formed, thus inhibiting this degradation pathway. Superoxide formation is only the first step of oxygen-mediated degradation of perovskite and although a material can generate more superoxide than another, it may be more sensitive to superoxide as reported previously.[24]

In 2013, Ku et al. introduced PSC with a mesoporous carbon layer in place of the metal back contact (herein termed mesoporous carbon perovskite solar cells; m-CPSC). These devices presented an improved stability in air and did not require vacuum evaporation of a metal back contact.[25] The m-CPSC architecture consists of three printed mesoporous layers deposited on a compact TiO_2 (c-TiO_2) layer, itself deposited on fluorine doped tin oxide (FTO) glass (**Figure 2**). The mesoporous titanium oxide (TiO_2) layer acts as the electron transport layer, a porous carbon layer plays the combined role of hole transport layer (HTL) and back contact, and an insulating zirconia oxide (ZrO_2) layer in between hinders electron–hole recombination. A perovskite solution is deposited through the carbon layer, infiltrating throughout the stack and annealed to crystallize the photoactive perovskite. These devices have shown reasonable stability thanks, at least in part, to the hydrophobic character of the carbon layer.[26] The lack of an expensive organic HTL such as 2,2′,7,7′-tetrakis[*N*,*N*-di(4-methoxyphenyl)amino]-9,9′-spirobifluorene and the absence of a metal back contact, usually thermally evaporated silver or gold, make these devices potentially low cost.[27] It has also been demonstrated that it is possible to screen-print the mesoporous layers over large areas making it suitable for mass production.[25,28–30] In the first demonstration, Ku et al. obtained a 6.6% PCE device stable over 840 h in the dark using MAPI perovskite. A year later, Mei et al. mixed MAPI with 5-aminovaleric acid [5-AVA, $NH_2(CH_2)_4CO_2H$] to improve the penetration and distribution of the perovskite within the stack which resulted in a $(5\text{-AVA})_x(MA)_{1-x}PbI_3$ based device with an improved PCE of 12.8%.[31] It was also suggested that this improved penetration and surface contact resulted in lower defect concentration.[24,31] 5-AVA affects the crystal structure of the MAPI by forming hydrogen bonds between its carboxyl (COOH) and ammonia (NH_3^+) groups and the iodide ions of MAPI.[31] These devices show promising stability with no performance drop after 1008 h under simulated sunlight without encapsulation.[31] In 2015, Li et al. presented a 12.8% PCE $(5\text{-AVA})_x(MA)_{1-x}PbI_3$ m-CPSC stable over 1000 h tested in air, at constant 1 sun illumination and a temperature of 80 °C.[32] The following year, Grancini et al. demonstrated an impressive 100 cm^2 m-CPSC with 3% 5-aminovaleric acid iodide [5-AVAI, $NH_2(CH_2)_4CO_2HI$] and with zero PCE loss over more than 10 000 h under ISOS standard conditions.[33] Their results suggest the presence of the 2D perovskite $(HOOC(CH_2)_4NH_3)_2PbI_4$ in the oxide scaffold with a 3D tetragonal phase of MAPI capping layer.[33] Density functional theory calculations and fluorescence measurements suggest the presence of a 2D/3D hybrid between the phases with a slightly wider bandgap than the 3D perovskite (1.7 and 1.6 eV, respectively).[33]

The addition of 5-AVA or 5-AVAI to the perovskite precursor solution clearly enhances the stability and efficiency of m-CPSCs. Whereas the latter has been explained in terms of improved morphology, penetration, and crystallization of the perovskite, the stability improvement origins are less clear.[31] In this paper, the stability of MAPI and aminovaleric acid methylammonium lead iodide (AVA-MAPI) in complete m-CPSCs and combinations of the mesoporous layers are investigated. Superoxide formation is

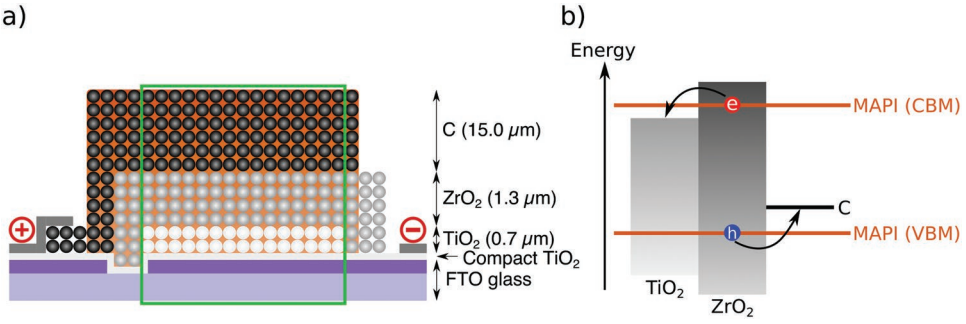

Figure 2. a) Schematic and b) band diagram of an m-CPSC. The photoactive area infiltrated with perovskite is highlighted in green.

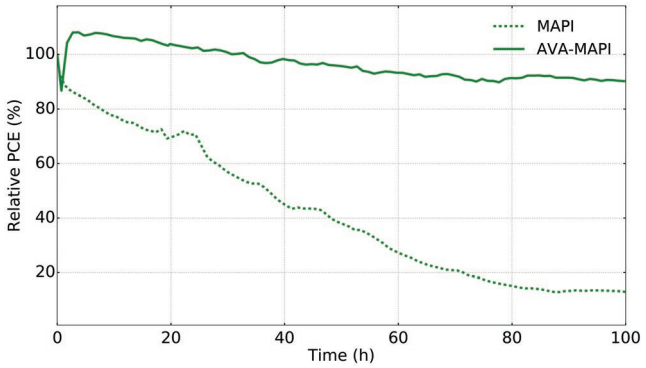

Figure 3. Power conversion efficiency of mesoporous carbon perovskite solar cells infiltrated with MAPI and AVA-MAPI perovskites in air at room temperature and under illumination for 100 h.

assessed by monitoring the fluorescence of 2-hydroxyethidium, product of dihydroethidium and superoxide.[34] We compare the superoxide yield results to the degradation rate in air under illumination obtained with in situ X-ray diffractometry (XRD).

2. Results and Discussion

Over 100 h under illumination at room temperature and in air, the m-CPSC infiltrated with the AVA-MAPI solution presents a much higher stability compared to the MAPI sample (10% PCE loss compared to 88%, respectively) (**Figure 3**). This shows the improved stability of AVA-MAPI compared to MAPI consistent with previous reports.[31,33]

The degradation rate in air and under illumination of MAPI and AVA-MAPI infiltrated in ZrO_2, TiO_2/ZrO_2, and TiO_2/ZrO_2/C was studied through the evolution of the ratio of the (110) peak of tetragonal MAPI and the (001) peak of trigonal PbI_2 peak under illumination (film side toward light source) over a period of 11 h (**Figure 4** and Figure S2, Supporting Information). MAPI infiltrated in ZrO_2 presents the highest degradation rate with the perovskite being almost entirely converted to lead iodide after 11 h. The same architecture using AVA-MAPI is much more stable in comparison with an I_{MAPI}/I_{PbI_2} ratio of 0.5 after 11 h indicating a significant amount of non-degraded perovskite. TiO_2/ZrO_2/MAPI shows a similar degradation rate

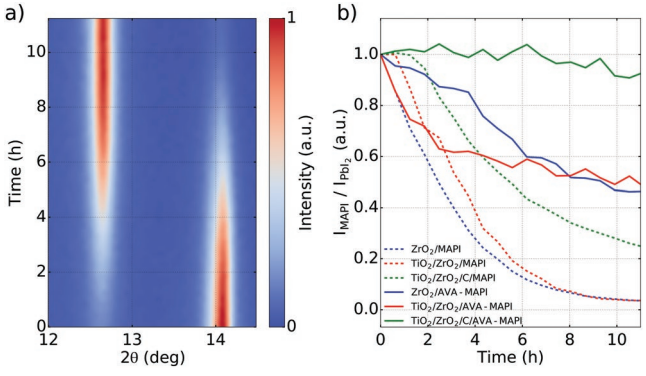

Figure 4. In situ XRD. a) XRD spectra between 12.0° and 14.5° of ZrO_2/MAPI and b) evolution of the peak intensity ratio I_{MAPI}/I_{PbI_2} over time.

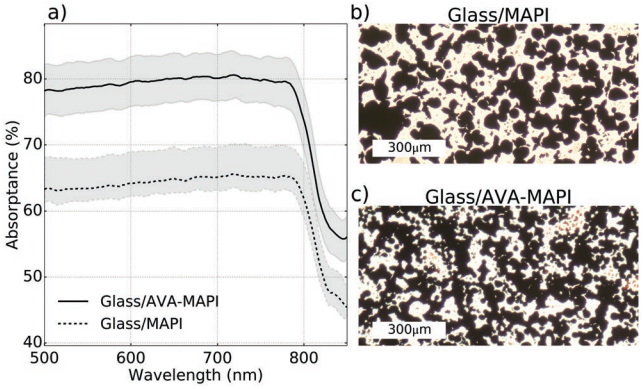

Figure 5. a) Absorptance (each curve is the average of four samples, the extremum values of all samples are indicated by the area around the curves) and bright-field microscopy of b) glass/MAPI and c) glass/AVA-MAPI samples.

to ZrO_2/MAPI and is also fully degraded after 11 h. TiO_2/ZrO_2/AVA-MAPI is initially less stable than ZrO_2/AVA-MAPI and displays a similar initial decay to ZrO_2/MAPI but slows after the first 2 h. TiO_2/ZrO_2/C stacks present higher stabilities than other samples using the same perovskite, likely thanks to inhibition of moisture degradation by the carbon layer. In particular, TiO_2/ZrO_2/C/AVA-MAPI shows the lowest degradation rate demonstrating the higher stability of AVA-MAPI compared to MAPI. AVA-MAPI infiltrated in any of the architectures studied here is therefore more stable than MAPI. In particular, AVA-MAPI infiltrated in ZrO_2 is less degraded after 11 h than MAPI infiltrated in the full stack of TiO_2/ZrO_2/C. This is somewhat surprising as it is expected that the thick carbon layer offers significant protection to the perovskite film. We believe this highlights the stability benefit of the 5-AVAI additive in air.

The superoxide formation of MAPI and AVA-MAPI was investigated by monitoring the fluorescence spectra of 2-hydroxyethidium. When drop-casted onto glass substrates the MAPI solution formed a film with large crystals while smaller crystals were obtained with the AVA-MAPI solution (**Figure 5**). Glass/AVA-MAPI absorbs more light than glass/MAPI partially owing to the slightly higher surface coverage (56% and 52%, respectively, 8% more). We note that absorptance is evident above 820 nm likely due to scattering. Whether the absorptance is corrected by shifting it so that the absorptance at 850 nm is zero, or not, does not significantly affect the corrected superoxide yield (Figures S15–S19, Supporting Information). The corrected superoxide yield $I(t)/I(t = 0)$ at 660 nm shows that glass/AVA-MAPI generates more superoxide than glass/MAPI on the timescale studied (**Figure 6**), consistent with the recent work of Lin et al.[24] Although AVA-MAPI has been reported to have a lower defect concentration than MAPI,[24] the smaller size of the crystals of AVA-MAPI lead to an increase surface/volume ratio which may increase the overall defect concentration of AVA-MAPI compared to MAPI, and thus may explain the higher superoxide yield measured. The variations of the probe fluorescence without a sample present were recorded twice as a baseline for our experiments. We observed a slight decrease of the fluorescence intensity over time which may be explained by the photodegradation of 2-hydroxyethidium.

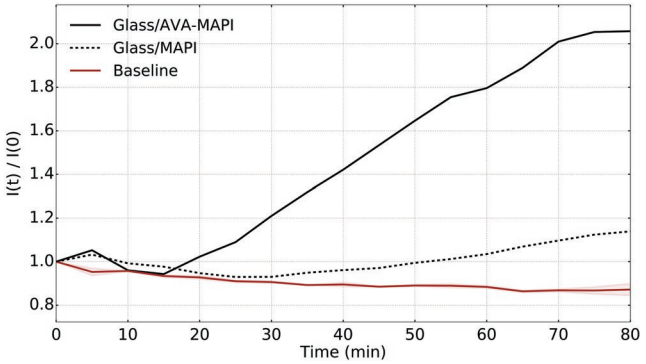

Figure 6. Superoxide yield of MAPI and AVA-MAPI drop-casted on glass with illumination through the perovskite layer ($\Delta\lambda_{exc} = \pm 3.5$ nm, $\Delta\lambda_{em} = \pm 10$ nm). The evolution of the superoxide yield without a sample is shown in brown. Correction factors β are given in Figure S13, Supporting Information.

The observed behavior of these perovskites infiltrated in mesoporous layers is significantly different than on glass. AVA-MAPI absorbs more light than MAPI in ZrO_2, and TiO_2/ZrO_2 mesoporous architectures, likely due to 5-AVAI improving the perovskite infiltration (**Figure 7**) and thus more perovskite being present in the mesoporous scaffold. Again, we also studied the superoxide yield in the case where the absorptance is assumed zero below the bandgap energy (Figures S15–S19, Supporting Information). The correction factors β for these samples are given in Figure S13, Supporting Information. **Figure 8** shows the superoxide yield of the MAPI and AVA-MAPI perovskite solutions drop-casted on ZrO_2, TiO_2/ZrO_2, and $TiO_2/ZrO_2/C$. Similar trends are observed independently of the direction of illumination (i.e., glass side or film side) other than for $TiO_2/ZrO_2/C$ samples. While superoxide formation is measured in these samples when illuminated through the glass, no or very little superoxide formation is observed when illuminated through the film side as the carbon top

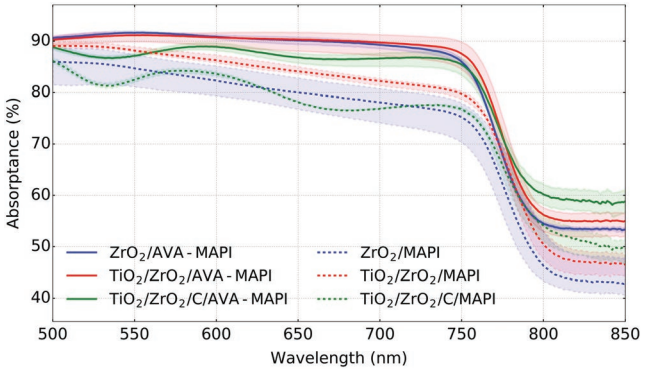

Figure 7. Absorptance of MAPI and AVA-MAPI and drop-casted on ZrO_2, TiO_2/ZrO_2, and $TiO_2/ZrO_2/C$ architectures measured through glass (see Figure S11, Supporting Information for the absorptance measured through the film, Figures S9 and S10, Supporting Information for the transmittance and reflectance, respectively) (each curve is the average of four samples). The transmittance of $TiO_2/ZrO_2/C$ was not measured due to its thick carbon layer and was assumed the same as TiO_2/ZrO_2 (the consequences of this assumptions on the correction factor and superoxide yield are discussed in Figure S12–S14, Supporting Information).

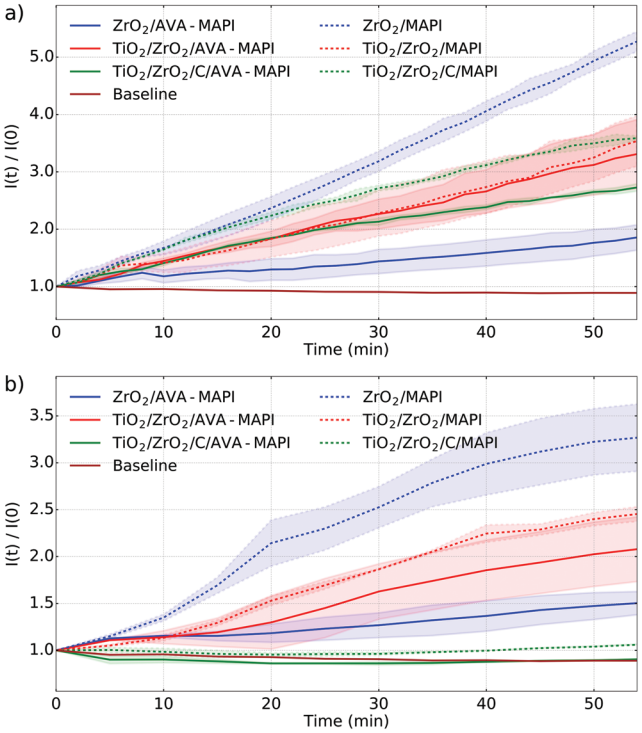

Figure 8. Superoxide yields of MAPI and AVA-MAPI drop-casted on ZrO_2, TiO_2/ZrO_2 and $TiO_2/ZrO_2/C$ architectures illuminated through a) the glass ($\Delta\lambda_{exc} = \pm 3.5$ nm, $\Delta\lambda_{em} = \pm 10$ nm) and b) the film ($\Delta\lambda_{exc} = \pm 3.5$ nm, $\Delta\lambda_{em} = \pm 3.5$ nm) (each curve is the average of two samples). Correction factors β are given in Figure S13, Supporting Information.

layer prevents the creation of excited carriers in the perovskite. $TiO_2/ZrO_2/C$ samples illuminated through the film are thus ignored for the rest of the discussion. We also note that the fluorescence intensity increase is not linear when the samples are illuminated though the film and this was due to exhaustion of the dihydroethidium probe (Figure S4, Supporting Information). Independently of the direction of illumination, ZrO_2/MAPI generates more superoxide compared to the other samples studied. When infiltrated in TiO_2/ZrO_2, the superoxide yield of MAPI decreases likely due to the possibility of charge injection into the mesoporous TiO_2. Little difference is observed between the superoxide yield of MAPI infiltrated in $TiO_2/ZrO_2/C$ and TiO_2/ZrO_2 when illuminated through the glass. The carbon layer is non-selective and therefore can extract holes and electrons. Lower electron concentration in the perovskite reduces the chance of superoxide formation, however one might expect lower hole concentration to result in reduced recombination with electrons, increasing the excited electron lifetime, therefore increasing the chance of superoxide formation (Figure 8a). AVA-MAPI infiltrated in ZrO_2 generates the lowest superoxide of all the samples studied independently of the illumination direction. TiO_2/ZrO_2/AVA-MAPI presents a higher superoxide yield than ZrO_2/AVA-MAPI and similar to TiO_2/ZrO_2/MAPI. This is quite surprising as a reduction in the superoxide yield may be expected due to the presence of the mesoporous TiO_2 layer as observed with MAPI, we attribute this, at least partly, to changes in morphology as discussed below. Repeat measurements showed that AVA-MAPI generates

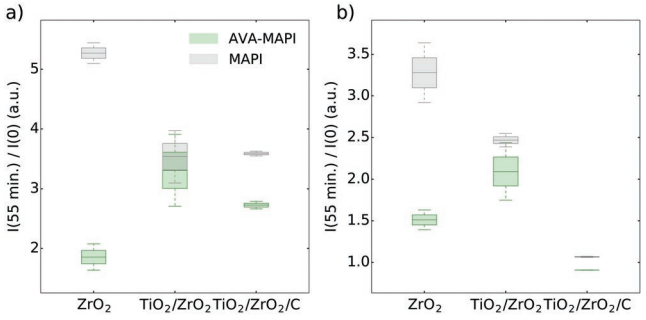

Figure 9. Comparison of the superoxide yield of MAPI and AVA-MAPI samples illuminated trough a) the glass and b) the film after 55 min (see Tables S1 and S2, Supporting Information for values).

less superoxide than MAPI when infiltrated in mesoporous TiO_2 (Figure S14b, Supporting Information). When illuminated through the glass substrate, $TiO_2/ZrO_2/C$/AVA-MAPI generates slightly less superoxide than in TiO_2/ZrO_2 but more than in ZrO_2 only (**Figure 9**). We note that given the difference in lamp power used during the superoxide measurement (1.5 mW cm^{-2}) and the XRD experiment (19 mW cm^{-2}), the results obtained in Figure 8 over 55 min are consistent with the ones obtained in Figure 4 during the first few minutes: AVA-MAPI samples present the lowest superoxide yield/highest stability, TiO_2/ZrO_2/MAPI is slightly more stable than ZrO_2/MAPI while TiO_2/ZrO_2/AVA-MAPI is less stable than ZrO_2/AVA-MAPI. The only difference with the superoxide experiment is observed for $TiO_2/ZrO_2/C$ architectures which are more stable than the other stacks and which can be explained by the presence of the carbon layer which prevents moisture infiltration and moisture-mediated degradation of the perovskite due to its hydrophobic properties.

The observed superoxide yield difference in ZrO_2 and TiO_2/ZrO_2 can be partially explained by the morphology of the samples (**Figure 10**). All samples present capping layers with similar morphologies, with the presence of larger (>10 µm) and smaller (<10 µm) grains (**Table 1**). In the case of AVA-MAPI, the smaller grains form a continuous and smooth capping layer on top of the mesoporous layers. The larger grains are a few µm thick and appear to be located inside the capping layer formed by the smaller grains and not sitting on top of it (Figure S6, Supporting Information). The smaller crystals in MAPI samples are bigger and do not form a smooth layer leaving many pinholes. Since AVA-MAPI forms smaller grains with ergo a higher defect concentration, we could expect the superoxide yield to be higher than in MAPI samples (as observed on glass). However, we believe, pinholes observed in MAPI samples allow increased oxygen diffusion into the samples while the compact capping layer formed in AVA-MAPI samples hinders oxygen diffusion. This may explain the higher superoxide yield observed in MAPI compared to AVA-MAPI in both ZrO_2 and TiO_2/ZrO_2 architectures. The higher superoxide yield measured in TiO_2/ZrO_2/AVA-MAPI compared to ZrO_2/AVA-MAPI could be explained by the increased surface roughness of TiO_2/ZrO_2/AVA-MAPI (especially for the observed dark spot) resulting in increased surface area to react with oxygen thus counterbalancing the reduction in the concentration of excited state electrons from charge injection.

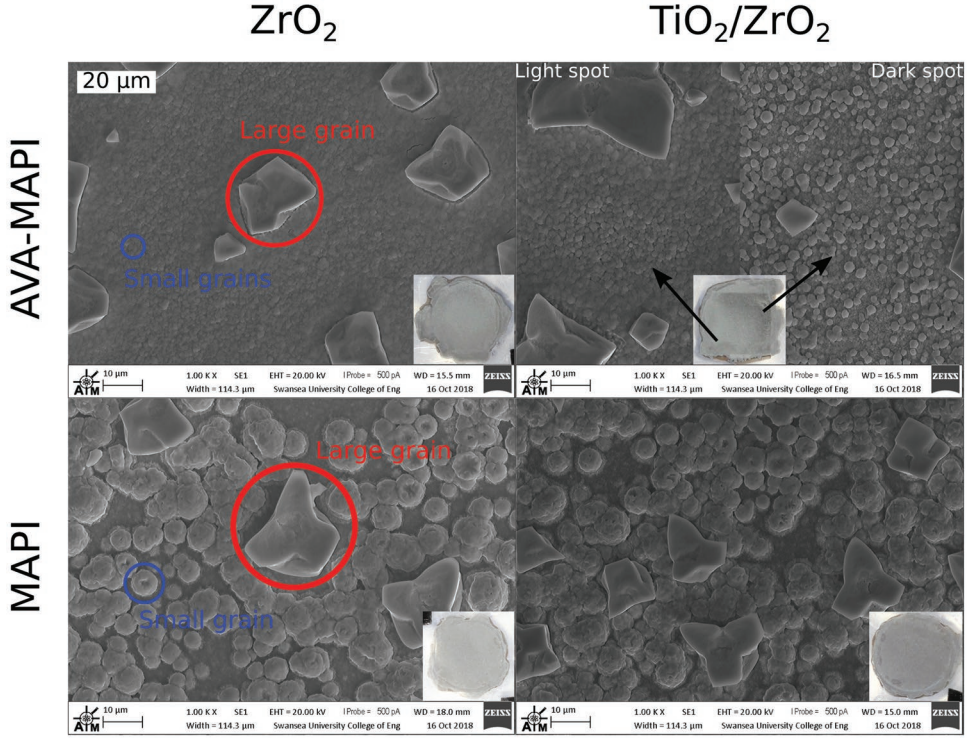

Figure 10. Top-down SEM images of the capping layer of MAPI and AVA-MAPI drop-casted in ZrO_2 with inserts showing a photograph of the sample. The TiO_2/ZrO_2/AVA-MAPI sample presented lighter and darker areas as indicated by the black arrows.

Table 1. Average perovskite large and small grain size in µm of MAPI and AVA-MAPI drop-casted in ZrO_2 and TIO_2/ZrO_2 calculated from 24 measurements for each image.

	Perovskite grain size in ZrO_2 [µm]		Perovskite grain size in TiO_2/ZrO_2 [µm]	
	Large	Small	Large	Small
AVA-MAPI	17.6 ± 3.0	1.2 ± 0.3	21.9 ± 7.8	1.6 ± 0.4
MAPI	15.2 ± 3.4	7.6 ± 2.4	11.8 ± 2.0	7.0 ± 1.3

See Figure S7, Supporting Information for more details.

The photoluminescence (PL) peak of ZrO_2/AVA-MAPI is slightly narrower (full-width-at-half-maximum ≈44 nm) than TiO_2/ZrO_2/AVA-MAPI (≈50 nm) indicating a lower trap states concentration in the former (Figure S8, Supporting Information). 5-AVAI has been previously shown to slow down the movement of perovskite iodide ions in the TiO_2/ZrO_2 architecture.[35] This may then limit trap state passivation (e.g., iodide ions passivating iodide vacancies) leaving more trap state to react with oxygen to form superoxide. This is consistent with the slower photobrightening observed in TiO_2/ZrO_2/AVA-MAPI samples compared to ZrO_2/AVA-MAPI (**Figure 11**). This needs to be put in perspective with passivation of trap states (and thus photobrightening) by superoxide and moisture. The photobrightening observed in Figure 11 is the result of ion migration, superoxide, and moisture. Ignoring the contribution of moisture, the slower photobrightening of the TiO_2/ZrO_2/AVA-MAPI sample indicates that passivation of trap states by superoxide is not enough to balance the slow ion migration. In both samples, large grains emit much less and photobrighten much slower than the small grains. Photodarkening of the small grains is observed in both samples and hints that the greater photobrightening in these grains is not due to higher enhanced trap state passivation by ion migration but rather trap state passivation by superoxide as the superoxide then degrades the perovskite. This is consistent with the higher defect concentration of small grains compared to large ones.

To further assess superoxide formation with respect to illumination direction, we studied further eight samples, namely MAPI and AVA-MAPI infiltrated in TiO_2/ZrO_2 (two samples of each, note new samples were used for each illumination direction) (**Figure 12**). Most excited charge carriers are localized within a few hundred nm in the film with respect to the illumination direction.[36] The superoxide yield does not change for MAPI depending on the illumination direction as oxygen can easily diffuse in the film and reacts where the excited charges were created. Conversely, less superoxide is formed when illuminating through the glass layer of AVA-MAPI than when illuminating from the film since the seemingly dense perovskite capping layer limits the rate of oxygen diffusion into the film. We believe this provides strong evidence for the increased oxygen diffusion in the MAPI samples and highlights the importance of the morphology in prevention of oxygen diffusion and hence superoxide formation. The processes and factors affecting superoxide formation are summarized in **Figure 13**.

3. Conclusion

We have studied the role of 5-AVAI in improving the stability of MAPI perovskite in m-CPSC. Changes in the perovskite and lead iodide XRD peak intensities under illumination showed higher degradation rates for MAPI samples than AVA-MAPI samples. Using dihydroethidium as a probe, the superoxide formation in MAPI and AVA-MAPI has been measured. AVA-MAPI deposited on glass presented a higher superoxide yield than MAPI. However, when drop-casted on ZrO_2, TiO_2/ZrO_2, and TiO_2/ZrO_2/C mesoporous architectures, AVA-MAPI presented significantly lower formation of superoxide than MAPI. We have shown that superoxide formation in these samples is the result of a combination of multiple factors including oxygen diffusion, grain morphology, and defect concentration. AVA-MAPI samples have smaller grains with higher surface/volume ratio and therefore more surface defects which are counterbalanced by an overall lower defect concentration through the binding of AVA to iodide vacancies, and poor oxygen diffusion into the film due to the compact perovskite layer, resulting in an overall lower superoxide yield. MAPI samples have larger grains with lower surface/volume ratio and thus less surface defects which are balanced by higher defect concentration compared to AVA-MAPI and the increased oxygen diffusion in the

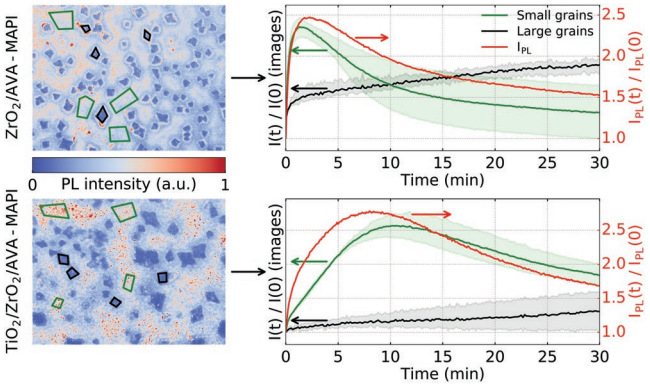

Figure 11. Fluorescence images of ZrO_2/AVA-MAPI and TiO_2/ZrO_2/AVA-MAPI samples and evolution of the intensity of the small grains (green), large grains (black), and the maximum spectral intensity I_{PL} over 30 min.

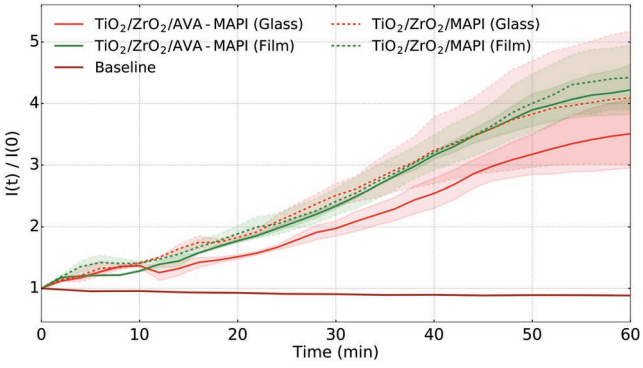

Figure 12. Superoxide yields ($\Delta\lambda_{exc}$ = 7 nm, $\Delta\lambda_{em}$ = 20 nm) of MAPI and AVA-MAPI infiltrated in TiO_2/ZrO_2 and illuminated through the glass and perovskite layer (each curve is the average of two samples).

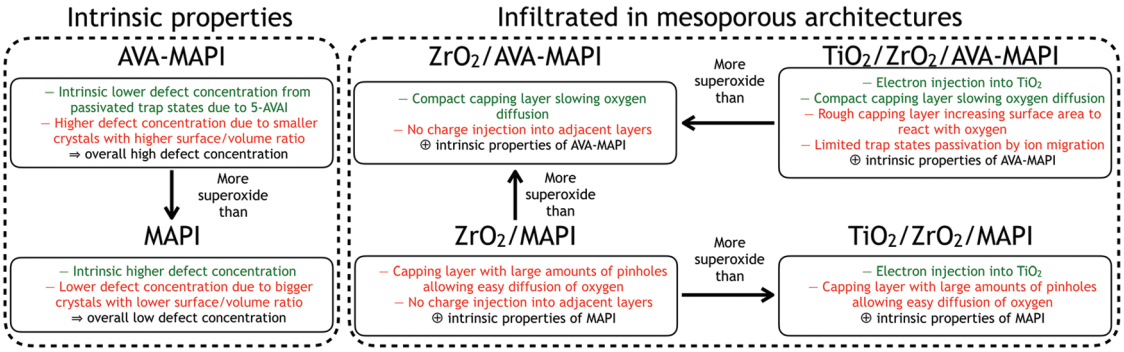

Figure 13. Summary of the processes happening in MAPI and AVA-MAPI on glass and infiltrated in ZrO_2 TiO_2/ZrO_2 mesoporous architectures (green: inhibiting effect, red: catalytic effect).

film caused by the very porous perovskite capping layer, leading to a higher superoxide formation yield. We have explained the lower superoxide yield measured when MAPI is infiltrated in the TiO_2/ZrO_2 architecture compared to the ZrO_2 architecture by the improved charge injection into the former architecture. Conversely, we observed a higher superoxide yield in TiO_2/ZrO_2/AVA-MAPI compared to ZrO_2/MAPI which we believe is due to the higher perovskite porosity observed in the former architecture. All these factors are heavily influenced by the sample morphology and thus better understanding and control of morphology is required to help to lower superoxide formation and thus increase the device stability.

4. Experimental Section

Sample Manufacturing: MAPI precursor solutions were prepared from a 1:1 molar solution of lead iodide (PbI_2, TCI) and MAI (Dyesol) in gamma-butyrolactone (Sigma-Aldrich). The AVA-MAPI solution was prepared as above for MAPI with the addition of 4% 5-AVAI, (Dyesol). In order to understand how each layer of the mesoporous structure affects the stability of the devices, a range of combinations of mesoporous layers was studied: ZrO_2 only, TiO_2, and ZrO_2, and the full stack of TiO_2, ZrO_2, and C, all deposited on FTO glass (**Figure 14**).

The samples were prepared by screen-printing commercially available pastes as described earlier.[28,29] The perovskite solutions were drop-casted on the different architectures, left at room temperature for 10 min, and then annealed at 50 °C for 1 h.

Power Conversion Efficiency Measurement: The current–voltage (*J–V*) curves of complete c-$TiO_2/TiO_2/ZrO_2$/C devices were recorded (Oriel Sol3A solar simulator) under simulated AM1.5 sun illumination. The stability of these devices was measured in air. Between each *J–V* measurement, the cells were kept at open circuit and under illumination under a 1 equiv. sun using a white LED. The cells were kept at room temperature during the experiment using a cooling system.

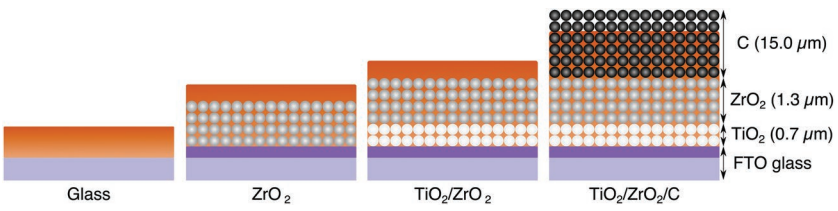

Figure 14. Schematic of the film architectures studied. ZrO_2 and TiO_2/ZrO_2 samples have a perovskite capping layer whereas full stacks did not (owing to the thickness of the carbon layer).

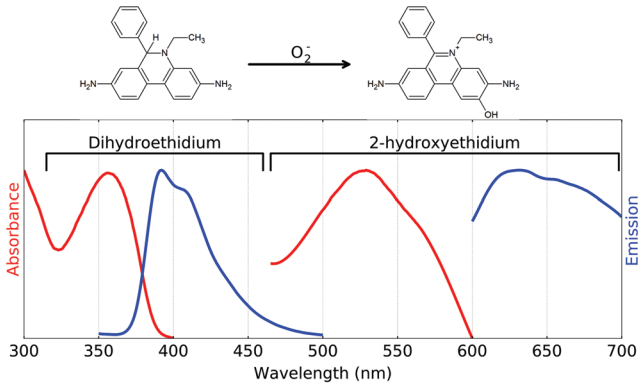

Figure 15. Illustration of the absorbance and fluorescence emission spectra of dihydroethidium (excitation wavelength $\lambda_{exc} = 289$ nm, excitation slitwidth $\Delta\lambda_{exc} = \pm 0.5$ nm, emission slitwidth $\Delta\lambda_{em} = \pm 2.5$ nm) and 2-hydroxyethidium ($\lambda_{exc} = 520$ nm, $\Delta\lambda_{exc} = \pm 3.5$ nm, $\Delta\lambda_{em} = \pm 10$ nm).

Spectrophotometry: The total (specular and diffuse) reflectance (%*R*) and transmittance (%*T*) were measured with a Perkin Elmer Lambda 750 spectrophotometer coupled with an InGaAs integrating sphere. The absorptance (%*A*) was then calculated as follows.

$$\%A = 100 - \%T - \%R \quad (1)$$

Fluorescence, Optical, and Electron Microscopy: The PL spectra and images ($\Delta\lambda_{exc} = 559$ nm, $\Delta\lambda_{em} = \pm 17$ nm) of the samples were recorded using an Olympus BX51 upright microscope coupled with an Olympus U-LH100HG mercury lamp, an Olympus XC10 camera, and an OceanOptics USB2000+ spectrometer. Optical microscopy was performed using an Olympus BH-2 bright-field microscope and electronic microscopy images were obtained with a Zeiss Evo LS25.

Superoxide Yield Measurement: A 39.4 µm probe stock solution was obtained by dissolving dihydroethidium (1.1 ± 0.1 mg, Sigma-Aldrich, ≥95%) in toluene (100 mL, Sigma-Aldrich, 99.8% or 99.9%). Samples were immersed into diluted dihydroethidium stock solution (10 mL, 3.94 µm) (**Figure 15**). An average value of 7641 ± 33 m^{-1} cm^{-1} was obtained at 357 nm for the extinction coefficient of dihydroethidium in toluene (comparable to the value of 9.75 × 103 m^{-1} cm^{-1} at 345 nm reported for dimethyl sulfoxide[37]) (Figure S3, Supporting Information). In order to generate superoxide, the samples were illuminated at ≈1.5 mW cm^{-2} with a Sylvania FVT 12v GY6,35 halogen lamp (**Figure 16**a) filtered with a 530 nm high pass filter and a near infrared filter to avoid degradation of the probe (Figure S1a, Supporting Information).

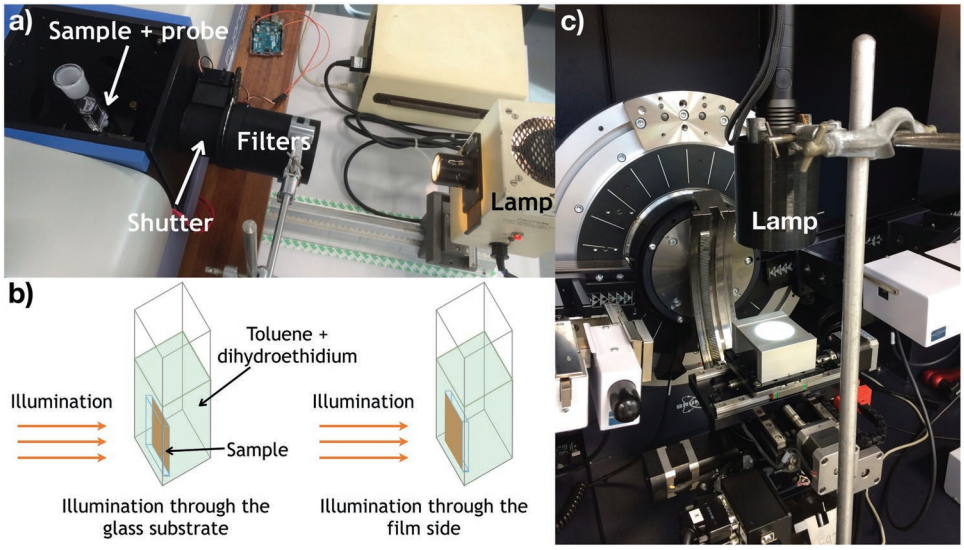

Figure 16. a) Superoxide setup. An external illumination source filtered with a 530 nm high pass and NIR filters is used to generate excited states in the sample. The sample is placed in a cuvette with 10 mL of dihydroethidium probe solution. The fluorescence of the probe solution is periodically measured using a fluorometer coupled with an automatic shutter. b) Schematic of the superoxide experiments during which samples were illuminated through the glass or through the film (i.e., the perovskite infiltration side), and c) XRD setup where a torch is used to illuminates the sample while the XRD pattern of the later is periodically measured.

The fluorescence spectra of 2-hydroxyethidium were measured with a HORIBA FluoroMax-4 fluorometer (λ_{exc} = 520 nm). The intensity ratio at 660 nm $I(t)/I(t=0)$ was used to monitor the superoxide yield (note that although this yield was used to compare samples, these are not absolute yields of superoxide formation). The superoxide yields are corrected for absorbance using[20]

$$\left[\frac{I(t)}{I(0)}\right]_{corr} = 1 + \frac{I(t) - I(0)}{\beta \cdot I(0)} \tag{2}$$

where β is a correction factor calculated from the total number of photons absorbed (and hence, the total number of excited charge carriers) by the sample

$$\beta = \frac{\int I_{lamp}(\lambda) \cdot A(\lambda) \cdot d\lambda}{S} \tag{3}$$

with $I_{lamp}(\lambda)$ the intensity of the lamp and $A(\lambda)$ the absorptance of the sample at wavelength λ, and S the area of the sample. The corrected superoxide yield is simply referred as $I(t)/I(t = 0)$ in the main text. Superoxide formation was studied with illumination through the glass substrate and through the film (Figure 16b).

In Situ XRD: XRD measurements were performed using a Bruker D8. In situ degradation was performed by illuminating the samples at ≈19 mW cm^{-2} with a LED Lenser M7R torch (≈19 mW cm^{-2}—about 13× higher than for the superoxide experiment—Figure 16c and Figure S1b, Supporting Information).[17] The compounds weight ratio evolution was then determined through the intensity ratio of the (110) tetragonal MAPI peak and the (001) PbI_2 peak using the relation[38]

$$I_{MAPI}/I_{PbI_2} \propto w_{MAPI}/w_{PbI_2} \tag{4}$$

where I_{MAPI} (I_{PbI_2}) is the intensity of the peak associated with MAPI (PbI_2) and w_{MAPI} (w_{PbI_2}) is its respective weight.

Data Analysis: Data were processed with Python[39] with the numpy,[40] scipy,[41] scikit-image,[42] and OpenCV[43] packages, and figures were generated using the matplotlib package.[44] Surface coverage of grains was calculated using image thresholding and grain sizes were measured using the ImageJ software.[45]

Supporting Information

Supporting Information is available from the Wiley Online Library or from the author.

Acknowledgements

The authors are grateful for the support of the EPSRC and Innovate UK for the SPECIFIC Innovation and Knowledge Centre and the European Regional Development Fund through the Welsh Government for support to the Sêr Solar program. M.L.D. is grateful for the financial support of the EPSRC (EP/R016666/1 and EP/S001336/1). M.L.D. and T.W. are grateful for funding through the EPSRC GCRF SUNRISE project (EP/P032591/1). E.V.P. is grateful for funding from Sêr Solar, the Swansea University, College of Engineering Zienkiewicz scholarship and the financial support provided by the M2A that has been made possible through funding from the European Social Fund via the Welsh Government. The authors would like to acknowledge the assistance provided by Swansea University College of Engineering AIM Facility, which was funded in part by the EPSRC (EP/M028267/1), the European Regional Development Fund through the Welsh Government (80708) and the Sêr Solar project via Welsh Government.

Conflict of Interest

The authors declare no conflict of interest.

Keywords

5-ammonium valeric acid iodide, AVA-MAPI, dihydroethidium, fluorescence, in situ x-ray diffractometry

Received: November 25, 2019
Revised: December 31, 2019
Published online:

[1] M. Yin, F. Xie, H. Chen, X. Yang, F. Ye, E. Bi, Y. Wu, M. Caib, L. Han, *J. Mater. Chem. A* **2016**, *4*, 8548.
[2] W. S. Yang, B.-W. Park, E. H. Jung, N. J. Jeon, Y. C. Kim, D. U. Lee, S. S. Shin, J. Seo, E. K. Kim, J. H. Noh, S. I. Seok, *Science* **2017**, *356*, 1376.
[3] Best Research-Cell Efficiency Chart, https://www.nrel.gov/pv/cell-efficiency.html (accessed: December 2019).
[4] A. Kojima, K. Teshima, Y. Shirai, T. Miyasaka, *J. Am. Chem. Soc.* **2009**, *131*, 6050.
[5] J. Burschka, N. Pellet, S.-J. Moon, R. Humphry-Baker, P. Gao, M. K. Nazeeruddin, M. Grätzel, *Nature* **2013**, *499*, 316.
[6] M. Liu, M. B. Johnston, H. J. Snaith, *Nature* **2013**, *501*, 395.
[7] N. J. Jeon, J. H. Noh, Y. C. Kim, W. S. Yang, S. Ryu, S. I. Seok, *Nat. Mater.* **2014**, *13*, 897.
[8] N. J. Jeon, J. H. Noh, W. S. Yang, Y. C. Kim, S. Ryu, J. Seo, S. I. Seok, *Nature* **2015**, *517*, 476.
[9] Y. C. Kim, N. J. Jeon, J. H. Noh, W. S. Yang, J. Seo, J. S. Yun, A. Ho-Baillie, S. Huang, M. A. Green, J. Seidel, T. K. Ahn, S. I. Seok, *Adv. Energy Mater.* **2016**, *6*, 1502104.
[10] M. Saliba, T. Matsui, K. Domanski, J.-Y. Seo, A. Ummadisingu, S. M. Zakeeruddin, J.-P. Correa-Baena, W. R. Tress, A. Abate, A. Hagfeldt, M. Grätzel, *Science* **2016**, *354*, 206.
[11] Y. Jinli, S. B. D. , D. Liu, T. L. Kelly, *ACS Nano* **2015**, *9*, 1955.
[12] J. A. Christians, P. A. Miranda Herrera, P. V. Kamat, *J. Am. Chem. Soc.* **2015**, *137*, 1530.
[13] A. Leguy, Y. Hu, M. Campoy-Quiles, M. I. Alonso, O. J. Weber, P. Azarhoosh, M. van Schilfgaarde, M. T. Weller, T. Bein, J. Nelson, P. Docampo, P. R. F. Barnes, *Chem. Mater.* **2015**, *27*, 3397.
[14] N. Aristidou, I. Sanchez-Molina, T. Chotchuangchutchaval, M. Brown, L. Martinez, T. Rath, S. A. Haque, *Angew. Chem., Int. Ed.* **2015**, *54*, 8208.
[15] N. Aristidou, C. Eames, I. Sanchez-Molina, X. Bu, J. Kosco, M. Saiful Islam, S. A. Haque, *Nat. Commun.* **2017**, *8*, 15218.
[16] S.-W. Lee, S. Kim, S. Bae, K. Cho, T. Chung, L. E. Mundt, S. Lee, S. Park, H. Park, M. C. Schubert, S. W. Glunz, Y. Ko, Y. Jun, Y. Kang, H.-S. Lee, D. Kim, *Sci. Rep.* **2016**, *6*, 38150.
[17] E. V. Péan, C. S. De Castro, M. L. Davies, *Mater. Lett.* **2019**, *243*, 191.
[18] R. Brenes, C. Eames, V. Bulović, M. S. Islam, S. D. Stranks, *Adv. Mater.* **2018**, *30*, 1706208.
[19] D. Bryant, N. Aristidou, S. Pont, I. Sanchez-Molina, T. Chotchunang atchaval, S. Wheeler, J. R. Durrant, S. A. Haque, *Energy Environ. Sci.* **2016**, *9*, 1655.
[20] S. Pont, D. Bryant, C.-T. Lin, N. Aristidou, S. Wheeler, X. Ma, R. Godin, S. A. Haque, J. R. Durrant, *J. Mater. Chem. A* **2017**, *5*, 9553.
[21] N. Aristidou, C. Eames, M. S. Islam, S. A. Haque, *J. Mater. Chem. A* **2017**, *5*, 25469.
[22] R. Brenes, D. Guo, A. Osherov, N. K. Noel, C. Eames, E. M. Hutter, S. K. Pathak, F. Niroui, R. H. Friend, M. S. Islam, H. J. Snaith, V. Bulović, T. J. Savenije, S. D. Stranks, *Joule* **2017**, *1*, 155.
[23] A. Walsh, D. O. Scanlon, S. Chen, X. G. Gong, S.-H. Wei, *Angew. Chem., Int. Ed.* **2015**, *54*, 1791.
[24] C.-T. Lin, F. De Rossi, J. Kim, J. Baker, J. Ngiam, B. Xu, S. Pont, N. Aristidou, S. A. Haque, T. Watson, M. A. McLachlan, J. R. Durrant, *J. Mater. Chem. A* **2019**, *7*, 3006.
[25] Z. Ku, Y. Rong, M. Xu, T. Liu, H. Han, *Sci. Rep.* **2013**, *3*, 3132.
[26] S. Ito, G. Mizuta, S. Kanaya, H. Kanda, T. Nishina, S. Nakashima, H. Fujisawa, M. Shimizu, Y. Haruyama, H. Nishino, *Phys. Chem. Chem. Phys.* **2016**, *18*, 27102.
[27] Y. Cai, L. Liang, P. Gao, *Chinese Phys. B* **2018**, *27*, 018805.
[28] J. Baker, K. Hooper, S. Meroni, A. Pockett, J. McGettrick, Z. Wei, R. Escalante, G. Oskam, M. Carnie, T. Watson, *J. Mater. Chem. A* **2017**, *5*, 18643.
[29] S. M. P. Meroni, Y. Mouhamad, F. De Rossi, A. Pockett, J. Baker, R. Escalante, J. Searle, M. Carnie, E. Jewell, G. Oskam, T. M. Watson, *Sci. Technol. Adv. Mater.* **2017**, *19*, 1.
[30] Y. Mouhamad, S. M. P. Meroni, F. De Rossi, J. Baker, T. M. Watson, J. Searle, E. H. Jewell, *Sol. Energy* **2019**, *187*, 129.
[31] A. Mei, X. Li, L. Liu, Z. Ku, T. Liu, Y. Rong, M. Xu, M. Hu, J. Chen, Y. Yang, M. Grätzel, H. Han, *Science* **2014**, *345*, 295.
[32] X. Li, M. Tschumi, H. Han, S. S. Babkair, R. A. Alzubaydi, A. A. Ansari, S. S. Habib, M. K. Nazeeruddin, S. M. Zakeeruddin, M. Grätzel, *Energy Technol.* **2015**, *3*, 551.
[33] G. Grancini, C. Roldán-Carmona, I. Zimmermann, E. Mosconi, X. Lee, D. Martineau, S. Narbey, F. Oswald, F. De Angelis, M. Graetzel, M. K. Nazeeruddin, *Nat. Commun.* **2017**, *8*, 15684.
[34] J. Zielonka, J. Vasquez-Vivar, B. Kalyanaraman, *Nat. Protoc.* **2008**, *3*, 8.
[35] A. Pockett, D. Raptis, S. M. P. Meroni, J. Baker, T. Watson, M. Carnie, *J. Phys. Chem. C* **2019**, *123*, 11414.
[36] R. Kerremans, O. J. Sandberg, S. Meroni, T. Watson, A. Armin, P. Meredith, *Sol. RRL* **2019**, 1900221.
[37] J. Zielonka, H. Zhao, Y. Xu, B. Kalyanaraman, *Free Radical Biol. Med.* **2005**, *39*, 853.
[38] A. Monshi, P. F. Messer, *J. Mater. Sci.* **1991**, *26*, 3623.
[39] G. van Rossum, *Python Tutorial*, Amsterdam **1995**.
[40] S. van der Walt, S. C. Colbert, G. Varoquaux, *Comput. Sci. Eng.* **2011**, *13*, 22.
[41] E. Jones, E. Oliphant, P. Peterson, Scipy: Open Source Scientific Tools for Python, http://www.scipy.org/ (accessed: December 2001).
[42] S. van der Walt, J. L. Schönberger, J. Nunez-Iglesias, F. Boulogne, J. D. Warner, N. Yager, E. Gouillart, T. Yu, *PeerJ* **2014**, *2*, e453.
[43] G. Bradski, *Dr. Dobb's J. Software Tools* **2000**,*120*, 122.
[44] J. D. Hunter, *Comput. Sci. Eng.* **2007**, *9*, 90.
[45] C. T. Rueden, J. Schindelin, M. C. Hiner, B. E. DeZonia, A. E. Walter, E. T. Arena, K. W. Eliceiri, *BMC Bioinformatics* **2017**, *18*, 529.